The Astrophysical Journal, 913:101 (17pp), 2021 June 1 https://doi.org/10.3847/1538-4357/abf2c1
© 2021. The American Astronomical Society. All rights reserved.

3D Convection-resolving Model of Temperate, Tidally Locked Exoplanets

Maxence Lefèvre[1], Martin Turbet[2], and Raymond Pierrehumbert[1]
[1] Department of Physics (Atmospheric, Oceanic and Planetary Physics), University of Oxford, Parks Road, Oxford, OX1 3PU, UK
[2] Observatoire Astronomique de l'Université de Genève, 51 chemin de Pégase, 1290 Sauverny, Switzerland
Received 2021 January 7; revised 2021 March 26; accepted 2021 March 27; published 2021 May 28

Abstract

A large fraction of known terrestrial-size exoplanets located in the habitable zone of M-dwarfs are expected to be tidally locked. Numerous efforts have been conducted to study the climate of such planets, using in particular 3D global climate models (GCMs). One of the biggest challenges in simulating such an extreme environment is to properly represent the effects of sub-grid convection. Most GCMs use either a simplistic convective-adjustment parameterization or sophisticated (e.g., mass flux scheme) Earth-tuned parameterizations. One way to improve the representation of convection is to study convection using numerical convection-resolving models (CRMs), with a fine spatial resolution. In this study, we developed a CRM coupling the non-hydrostatic dynamical core Advanced Research Weather-Weather Research and Forecast model with the radiative transfer and cloud/precipitation models of the Laboratoire de Météorologie Dynamique generic climate model to study convection and clouds on tidally locked planets, with a focus on Proxima b. Simulations were performed for a set of three surface temperatures (corresponding to three different incident fluxes) and two rotation rates, assuming an Earth-like atmosphere. The main result of our study is that while we recover the prediction of GCMs that (low-altitude) cloud albedo increases with increasing stellar flux, the cloud feedback is much weaker due to transient aggregation of convection leading to low partial cloud cover.

Unified Astronomy Thesaurus concepts: Exoplanet atmospheres (487); Atmospheric clouds (2180)

1. Introduction

The habitable zone (HZ) is classically defined as the range of orbital distances for which a planet can sustain water in liquid phase at the surface Kasting et al. (1993), providing a potentially suitable environment (surface, liquid water, photons) for the emergence of life as we know it on Earth. Depending on the rotation state and the atmospheric composition of the planet, various processes can either extend or narrow the HZ. While the presence of greenhouse gases tends to increase the surface temperature, the radiative effect of clouds can be much more subtle. Clouds can scatter (and thus reflect) as well as absorb a significant part of incident stellar radiation. But they can also absorb (and scatter) the infrared thermal emission from the surface and the atmosphere, and then reemit (or back scatter, respectively) infrared thermal radiation back to the surface.

On Earth, the relative ratio between cloud-free and cloudy area in the tropics have a strong effect on the mean temperature (Pierrehumbert 1995). It is therefore crucial to know the composition, thickness, and vertical and horizontal spatial distributions of these clouds to correctly evaluate the state of the climate of the Earth and by extension of other planets in or outside of the solar system.

Most terrestrial-size exoplanets located in the HZ that have been detected so far (Anglada-Escudé et al. 2016; Gillon et al. 2017; Bonfils et al. 2018; Tuomi et al. 2019; Zechmeister et al. 2019) are orbiting around low mass stars, also known as M-stars, the most abundant and longest-lived stars in the Milky Way (Kirkpatrick et al. 2012). A significant number of the planets orbiting in the HZ of low mass stars are expected to have near-zero obliquity and be in synchronous rotation around their host star (i.e., with one side of the planet permanently facing its host star). On a synchronously rotating telluric exoplanet covered with water, the constant stellar radiation received at the substellar point should create a strong convective region producing very thick clouds reflecting the stellar light (Yang et al. 2013). This behavior has been shown to be robust across a wide range of three-dimensional global climate models (GCMs; Yang et al. 2019b). The more irradiation a synchronous planet receives, the stronger the moist convection and thus the more reflective the substellar cloud cover is (Yang et al. 2013). As a result, the inner edge of the HZ for synchronously rotating planets was found to lie significantly closer to the host star (Yang et al. 2013). This mechanism may be less effective for synchronous planets in the fast-rotating regime, i.e., with orbital periods roughly lower than 10 days (Edson et al. 2011; Haqq-Misra et al. 2018). For these planets, winds are strong enough to shift the clouds away from the substellar point (Kopparapu et al. 2016), thus reducing the effective cloud coverage in the substellar region, where the peak of instellation is. This effect weakens the cloud feedback described above (Kopparapu et al. 2016). This effect highlights the importance of knowing accurately the composition, thickness, as well as the vertical and horizontal distributions of clouds on a synchronously rotating planet to get insight into its mean climate state.

The representation of clouds and turbulence in the GCMs is one of the most important uncertainties of these models. In fact, the typical size of the structures of these phenomena, i.e., the shallow convection cells diameter, varies on Earth from 10–40 km (Atkinson & Wu Zhang 1996). This is much lower than the typical horizontal resolution of GCMs (∼100 km). GCMs therefore use sub-grid parameterizations to represent the effects of convection and turbulence, which is a main source of uncertainty in the models (Fauchez et al. 2020; Yang et al. 2019b). In fact, these schemes are either (i) too simple to represent the mixing of wind, energy, and tracer by the convection, or either (ii) sophisticated, but tuned to simulate present-day Earth, and can therefore give inaccurate results

when used to simulate environments very different from the Earth, such as planets in synchronous rotation. To be able to resolve convection in such exotic environments (in order to better understand them), it is necessary to run models at a spatial resolution similar to that at which convection processes operate.

Correctly modeling convection on synchronously rotating planets is not only crucial to their mean climate state and thus their potential habitability, but is also key to the observability of these planets in reflected light. Direct imaging in reflected light is indeed one of the most promising avenues to detect and characterize temperate, Earth-size planets orbiting around nearby stars. Specifically, it has been shown that the reflected light of very nearby temperate planets such as Proxima b (Anglada-Escudé et al. 2016) could be detected and analyzed with Extremely Large Telescope class telescopes (Turbet et al. 2016). Lovis et al. (2017) even proposed that, combining direct imaging with high-resolution spectroscopy on an 8 m class telescope, observations of Proxima b, in particular in reflected light could be attempted. However, our ability to detect and characterize Proxima b (and its atmosphere, surface, and clouds) depends strongly on the amount of light reflected by the planet. This amount highly depends on the reflectivity of the cloud cover (especially near and eastward of the substellar region), where the signal measured by direct imaging is more favorable.

On Earth intense convective activity occurs in the tropics leading to a cloud coverage of about 70% above the oceans (Eastman et al. 2011; Stubenrauch et al. 2006). Several types of clouds play a distinct role in that net coverage. In the tropics the low-altitude stratocumulus covers 20% of the surface, mesoscale high opaque clouds 6%, and cirrus clouds about 45%. Since the 1980s, some models have been developed with the aim to study the convection (Lipps & Hemler 1986, 1988) and its organization (Held et al. 1993). With the evolution of computing capacity, the model evolved from two-dimensional models (Grabowski 2001; Grabowski & Moncrieff 2002) to three-dimensional channel configuration models (Tompkins 2001; Wing & Cronin 2016), and last to periodic three-dimensional models (Tompkins 2001; Muller & Held 2012; Wing & Emanuel 2014). From observation campaigns (Tobin et al. 2013) and numerical modeling, several convective and squall line and self-aggregation clusters where clouds occupy only a limited area have led to a drier free troposphere and larger domain-mean outgoing longwave radiation (Wing et al. 2017). Self-aggregation is also obtained in aquaplanet with GCMs and parameterized convection (Bony et al. 2016), resulting in the control of the anvil cloud fraction by the sea surface temperature (SST), and a warmer SST leads to less anvil cloud fraction.

Zhang et al. (2017) performed the first modeling effort to study the convective activity in synchronously rotating planets orbiting around M-stars. With a 3 km resolution and GCM generated boundary conditions, using radiative transfer and microphysics designed to study Earth this model investigated only one incident flux value of 2000 $W\,m^{-2}$. Sergeev et al. (2020) also studied the convection on Proxima Centauri b using a GCM with a zoom at the substellar point, lowering the resolution down to 4 km covering 40° of latitude and longitude. Sergeev et al. (2020) focused on the impact of resolved convection on the large-scale dynamics for one single stellar flux and rotation rate and also on the comparison between the resolved convection and two different GCM convection parameterizations. Here, we propose to study the convection regime of tidally locked environment using convection-resolving modeling with a realistic radiative transfer and water cloud microphysics. Most simulations were run for the case study of the temperate, terrestrial-mass exoplanet Proxima b, because we were motivated by its high potential for future direct imaging observations. However, we explore broader cases than just Proxima b, by first varying the spectral type of the host star, then varying the strength of the stellar flux and last varying the rotation period of the planet (to recover cases simulated in Yang et al. 2013). The main goal of our study is to understand how the convection behaves at the substellar point of aquaplanets in synchronous rotation. This is a promising pathway to derive realistic parameterizations of the convection as well as the clouds albedo impacting Bond albedo of such planets.

The paper is organized as follows. Our convection-resolving model (CRM) is described in Section 2. In Section 3, the reference simulation is presented. The impact of the incident stellar flux and rotation rate are discussed in Sections 4 and 5, respectively. The results are discussed in Section 6 and our conclusions are summarized in Section 7.

2. The Laboratoire de Météorologie Dynamique Generic CRM

2.1. Dynamical Core

This study is conducted using the fully compressible non-hydrostatic dynamical core of the Advanced Research Weather-Weather Research and Forecast (hereafter referred to as WRF) terrestrial model (Moeng et al. 2007; Skamarock & Klemp 2008). The large-eddy simulation (LES) mode is used: the grid spacing of the WRF model is refined to resolve the largest turbulent eddies responsible for most of the energy transport by buoyant convection (Lilly 1962; Sullivan & Patton 2011). Such a modeling technique has been used to study Earth convection and small-scale turbulence. Atmospheric turbulence modeling has been conducted on various planets with WRF: on Mars (Spiga et al. 2010), on Venus (Lefèvre et al. 2017, 2018), and an exoplanetary environment (Zhang et al. 2017). Sub-grid-scale "prognostic turbulent kinetic energy" closure by Deardorff (1972) is used to parameterize turbulent mixing by unresolved small-scale eddies as in Moeng et al. (2007).

2.2. Coupling with Complete Laboratoire de Météorologie Dynamique Generic GCM Physical Packages

The WRF core was coupled to the Laboratoire de Météorologie Dynamique (LMD) generic physics package in a similar way to that of the LMD Mars mesoscale model (Spiga & Forget 2009) and the LMD Venus mesoscale model (Lefèvre et al. 2018, 2020). Due to timescale of the convection and clouds dynamics, the LMD generic CRM uses an online radiative transfer and is therefore a category 3 LES (according to the terminology described in Section 2.4 of Spiga et al. 2016). The LMD generic physics model is a versatile package that has been used on various studies with the LMDz 3D dynamical core from low irradiated planets terrestrial planets such as Archean Earth (Charnay et al. 2013), Early Mars (Forget et al. 2013; Wordsworth et al. 2013; Turbet et al. 2017a, 2020; Turbet & Forget 2019), Snowball Earth-like

planets or exoplanets (Turbet et al. 2017b), as well as for terrestrial exoplanets receiving a similar flux than Earth (Wordsworth et al. 2011; Bolmont et al. 2016; Turbet et al. 2016, 2018; Auclair-Desrotour et al. 2019), and for terrestrial exoplanets receiving relatively high irradiation such as future Earth (Leconte et al. 2013b) or tidally locked exoplanets (Leconte et al. 2013a). The LMD generic physics model has also been used to simulate the atmosphere of solar system giant planets (Spiga et al. 2020) and warm-Neptune-like exoplanets (Charnay et al. 2015a, 2015b).

The radiative transfer of the LMD generic physics package uses the correlated-k method (Eymet et al. 2016) for various species like CO_2, N_2, and H_2O. The radiative effect of clouds and Rayleigh scattering are taken into account. The incident stellar spectrum can be chosen to represent any type of host star. The spectrum used for Proxima Centauri (the star) was computed using the synthetic BT-Settl spectrum (Rajpurohit et al. 2013) for a M 5.5 star, with $T_{\rm eff} = 3000$ K, $g = 10^3$ m s^{-2} and [M/H] = 0.

Melting, freezing, condensation, evaporation, sublimation, and precipitation of H_2O are included in the model. Water cloud particle sizes are determined from the amount of condensed material and the number density of cloud condensation nuclei set to 10^6 kg^{-1} for liquid water clouds and to 10^4 kg^{-1} for water ice clouds (Leconte et al. 2013b). Due to the small size of the grids in the CRM, typically from tens of meters to about 1 km, the cloud fraction of a grid cell can be only be either 0% or 100%. The sedimentation of ice particles and liquid droplets is computed following a modified Stokes law (Rossow 1978). Precipitation of water is performed with the Boucher et al. (1995) scheme. Evaporation of precipitation is also taken into account.

The purpose of this is paper to study the convection and clouds on temperate, tidally locked aquaplanets with a focus on the exoplanet Proxima b. From the radial velocity measurements of Anglada-Escudé et al. (2016), Proxima b is likely a rocky planet with a most probable mass of 1.4 $M_\oplus$. We assumed that the density of the planet is similar to Earth (5500 kg m^{-3}) and that the radius of the planet is equal to 7160 km (1.1 $R_\oplus$) as in Turbet et al. (2016). The surface gravity is thus equal to 10.9 m s^{-2} for the fast rotation regime and 13.72 m s^{-2} for the slow rotation regime defined in the next subsection. The first value is the actual value of Proxima b from the mass and radius measurements, and the second value is to facilitate a comparison with Yang et al. (2014). No obliquity and a circular orbit and a flat topography were assumed. The planet is assumed to be in synchronous rotation. The atmospheric composition is assumed to be close to the present-day Earth, i.e., N_2-dominated with 376 ppm of CO_2. The mixing ratio of H_2O can vary in space and time.

To ensure that the model is able to resolve realistic convective activity and clouds, it has first been tested using data from tropical convection collected during the Tropical Ocean-Global Atmosphere Coupled Ocean-Atmosphere Response Experiment (Webster & Lukas 1992), aka the TOGA-COARE campaign. The convection resulting from the model (see the Appendix) consists of a shallow convection from the surface to 700 hPa (about 2.5 km) and deep convective plumes reaching 100 hPa (about 17 km). These altitudes are close to what has been measured during the campaign, and the associated surface rain over the simulated domain can reach up to 25 mm day^{-1}, close to the mean surface rain value observed in that TOGA-COARE region (Johnson et al. 2002) and in the tropics in general (Kikuchi & Wang 2008). With a simple microphysical model and configuration that are not tuned for Earth, the model is able to resolve realistic tropical convection.

2.3. Simulation Setup

The initial mean vertical profiles of atmospheric fields (temperature, pressure, winds, and water) in the CRM were taken from LMD generic GCM simulations of Proxima b from Turbet et al. (2016). Specifically, we extracted the mean vertical profiles at the substellar point, averaged over 20 consecutive Earth days. To explore different convective regimes, various incident stellar flux were considered, from 800 W m to 1280 W m^{-2}, as well as two rotation speeds, 6.3 10^{-6} and 1.1 10^{-6} s^{-1} corresponding to rotation periods of 11 and 60 Earth days, respectively. The 11 day rotation period (relatively fast rotation regime) was chosen to fit the case of Proxima b. The 60 day rotation period (slow rotation regime) was chosen to fit the main case of Yang et al. (2013). Note that in the GCM the maximum of the cloud fraction does not occur at the substellar point because of atmospheric dynamics and that this specific position may be different for another GCM. Figure 1 shows the vertically integrated time-averaged cloud fraction in the GCM for the different cases of incident flux and rotation rate.

The position of the maximum cloudiness is close to the equator, therefore, no Coriolis effect is considered in the CRM runs. To take into account the heating/cooling from the large-scale circulation of the atmosphere, a heating rate profile extracted from GCM runs is added up to the temperature tendency from the physics package, in a similar way to that in Lefèvre et al. (2017, 2018), called advection heating rate hereafter. These profiles are time averaged and constant during the time of the simulations. On tidally locked planets two circulation regimes prevail: equatorial super-rotating jet or substellar/anti-substellar circulation. The equilibrium depends on the the equatorial Rossby deformation radius (Leconte et al. 2013a). Only the effect of the large-scale circulation on the temperature is considered in this study. For the planets considered in our study, i.e., an N_2-dominated atmosphere with a surface temperature of around 300 K with a planetary radius close to the Earth, the atmospheric circulation falls into the two regimes. For an 11 day rotation period, the planetary atmosphere is in an equatorial super-rotating jet regime with planetary-scale waves interactions (Showman & Polvani 2011; Hammond & Pierrehumbert 2018). For a 60 day rotation period, the equatorial Rossby deformation radius exceeds the planetary radius and therefore a planetary Rossby wave would be bounded by this radius, and thus the substellar/anti-substellar circulation dominates the large-scale circulation. This difference in circulation reverberates to differences in the advection heating rates, in particular between 15 and 25 km (see Figure 2), and exhibits the greater efficiency of heat transport for slow rotators. A time-averaged GCM vertical profile of zonal and meridional winds is prescribed.

The general circulation therefore dominates the advection heating in the upper atmosphere, while closer to the surface it is the convection. These rates are time averaged from the GCM simulation, however, to avoid any influence from the moist convective scheme used in the GCM physics package and let the resolved convection in the CRM be free to equilibrate, the

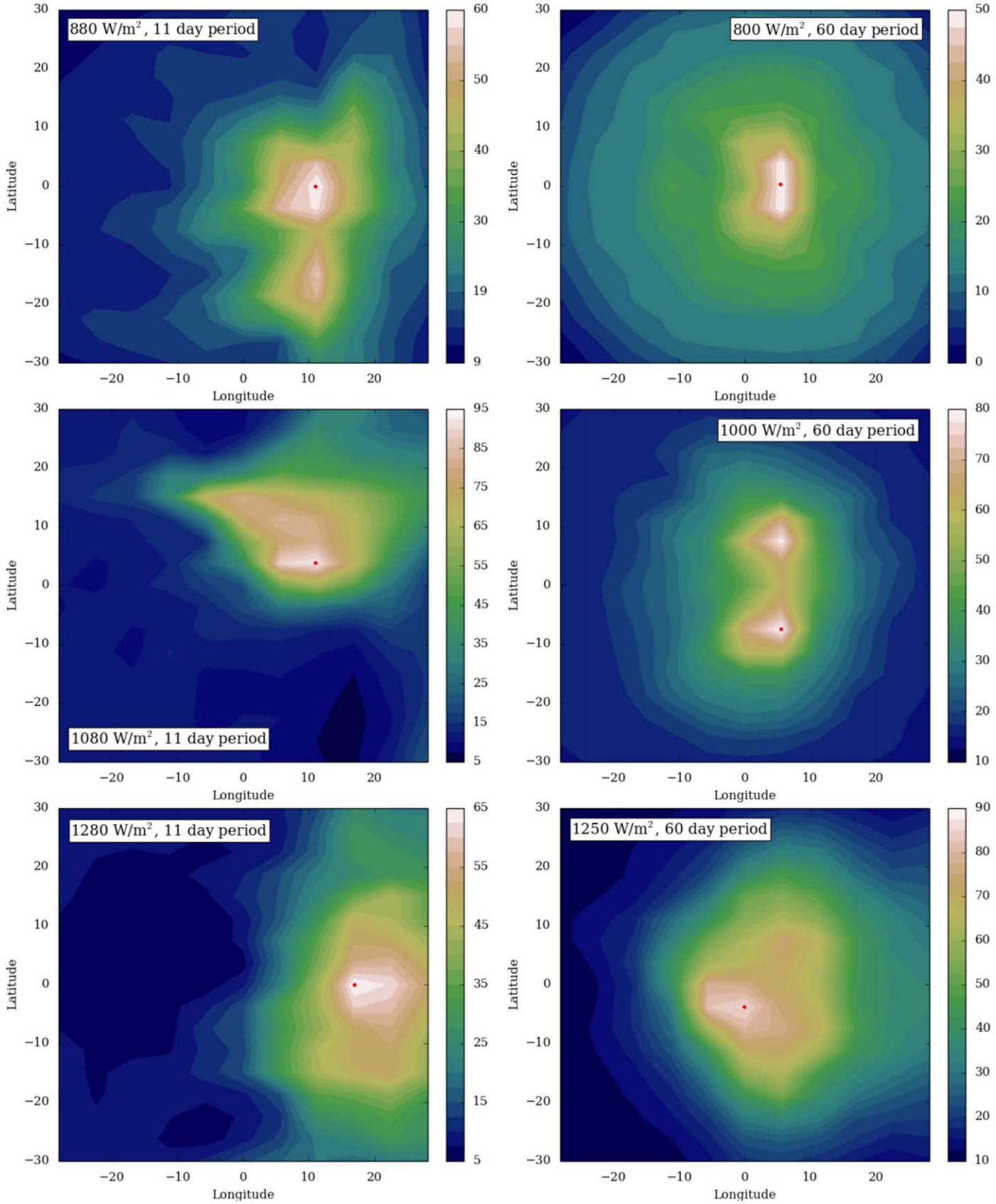

Figure 1. Vertically integrated time averaged over 20 days of aerosol opacity in the GCM for an incident of 880 W m^{-2} and 11 day rotation period (top left panel), 1080 W m^{-2} and 11 day rotation period (middle left panel), 1280 W m^{-2} and 11 day rotation period (bottom left panel), 800 W m^{-2} and 60 day rotation period (top right panel), 1080 W m^{-2} and 60 day rotation period (middle right panel), and 1250 W m^{-2} and 60 day rotation period (bottom right panel). The red dot refers to the position where the initial profiles are extracted.

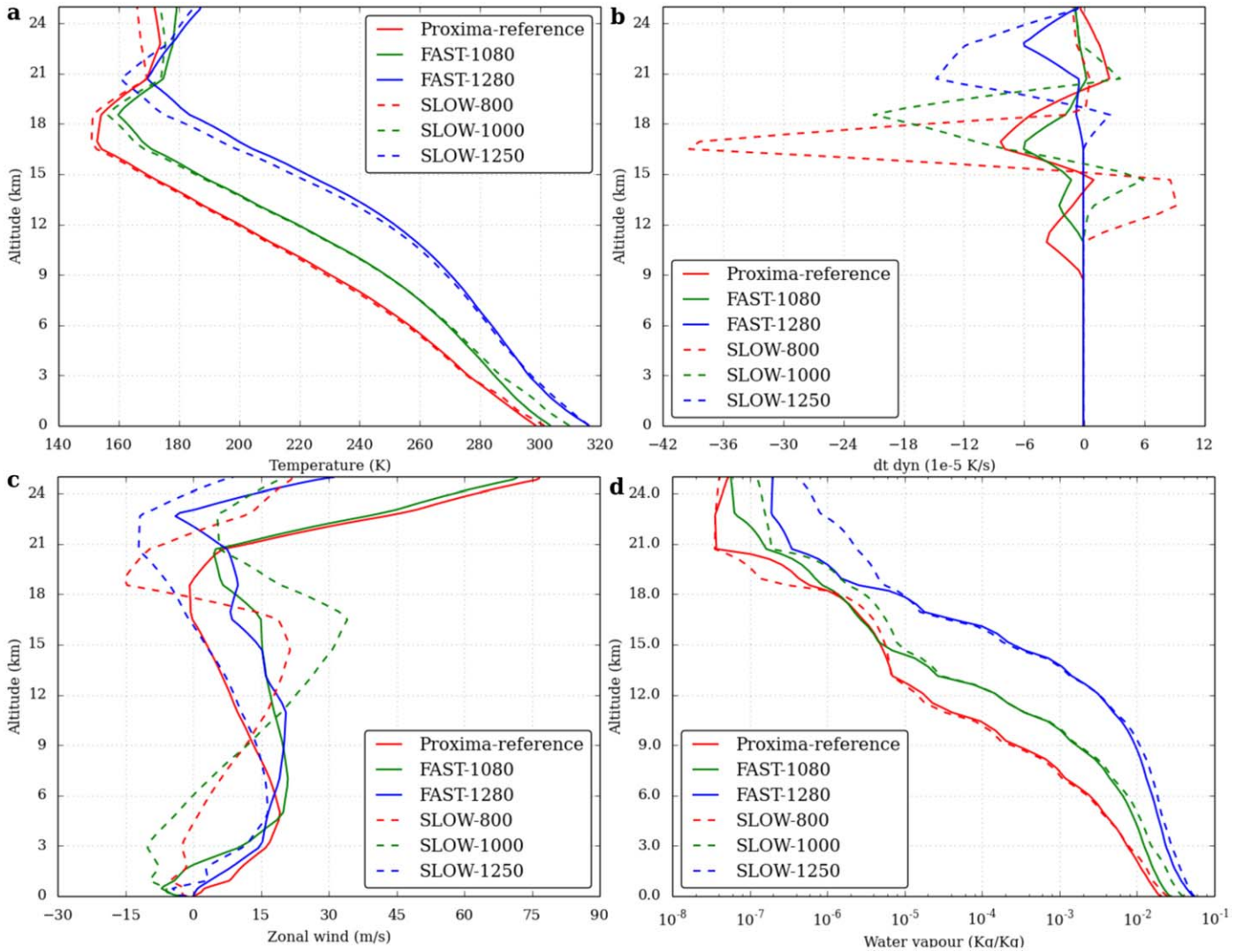

Figure 2. Initial vertical profile of the atmospheric temperature in Kelvin (a), advection heating rate in Kelvin per second (b), zonal wind in meter per second (c) and water vapor in kilogram per kilogram of air (d) for the six cases of stellar insolations and rotation rates considered in our study (see Table 1). These profiles are time-averaged GCM outputs at the maximum of column water cloud fraction (Figure 1). The constant value of the large scale from the surface to approximately 9 km is set to 10^{-6} K s^{-1} (see the text).

advection heating rate profile is set to a constant value of -1×10^{-6} K s^{-1} from the surface to approximately 9 km, representative of the cooling of the atmosphere at this altitude. Figure 2(a) displays the initial temperature profile (Kelvin), Figure 2(b) the advection heating rate vertical profile (in 10^{-5} K s^{-1} units), Figure 2(c) the initial zonal wind profile (meter per second) and Figure 2(d) the initial water vapor vertical profile (kilogram per kilogram of air). The atmosphere is assumed to be initially cloud-free. The stellar fluxes for the two rotation rates are slightly different to ensure a similar surface temperature, which is expected to be the main driver of the convection and a key factor of the organization of the convection. Three sets of initial surface temperatures (calculated with the GCM simulations) are considered: 295, 305, and 315 K at the substellar point. As shown in Figure 1 with the red dots, the extracted profiles are not at the substellar point and so the surface temperatures differ over a few Kelvins from the reference surface temperature. The surface temperature is free to evolve during the simulation. The bottom boundary is an oceanic surface with a 0.07 albedo. The planetary and atmospheric parameters for the different cases considered are summed up in Table 1.

The horizontal grid size is 1 km over 250×250 km to be able to revolve large convective cells, between two and three times the size of the LMD generic GCM cells at the equator. We use a double periodic domain. The vertical domain extends from the surface to 25 km of altitude, about 900 Pa, to ensure that the convective plumes are able to reach their equilibrium levels. The number of vertical points is set to 80. A Rayleigh sponge layer is set at the top of the domain with a 1 km depth and a damping coefficient of 0.01 s^{-1} to avoid spurious reflection of upward-propagating gravity waves (Klemp et al. 2008). The different cases are run over about 10 Earth days.

3. Results of the Reference Simulation

We present in this section the results of our reference simulation, corresponding to the parameters (spectral insolation, mass, rotation rate, etc.) chosen to best reproduce the exoplanet Proxima b (corresponding to the first case in Table 1).

Table 1
Planetary and Atmospheric Parameters for the Different Simulations

Parameter	Value			
Heat capacity ($J\,K^{-1}$)	1000			
Surface pressure (Pa)	10^5			
Composition	N_2-dominated, CO_2 : 376 ppm, H_2O: variable amount (Figure 2)			
Obliquity	0			
Eccentricity	0			
Case	Stellar type	Incident flux ($W\,m^{-2}$)	Rotation period (days)	Gravity ($m\,s^{-2}$)
Proxima b (reference)	M5.5	880	11	10.97
FAST-1080	M5.5	1080	11	10.97
FAST-1280	M5.5	1280	11	10.97
SLOW-800	M2	800	60	13.72
SLOW-1000	M2	1000	60	13.72
SLOW-1250	M2	1250	60	13.72

Figure 3 shows three snapshots of resulting vertical wind field (meter per second) after about 30 hr of simulations: a vertical cross section (a) and a horizontal cross section at 1 km altitude (c) and 20 km altitude (c). Shallow convection is visible below 3 km with cells between 20 and 50 km in diameter and vertical wind reaching $\pm 8\,m\,s^{-1}$, slightly above Earth shallow convection values at the same altitude (Schumacher et al. 2015; Giangrande et al. 2016). At 2.5 km, the typical vertical wind ranges between $\pm 1.5\,m\,s^{-1}$, three times the values at this altitude in the Sergeev et al. (2020) study. This difference is due to the thickness of the shallow convection, which is thicker in the present study. The diameter of these cells is comparable to that of Earth shallow convection cells (Atkinson & Wu Zhang 1996). From 5 km to approximately 19 km (about 40 mbar), deep convection occurs with vertical wind reaching up to $40\,m\,s^{-1}$. On Earth, deep convective plumes reach the tropopause at typically 15 km with vertical wind speed up to $20\,m\,s^{-1}$ (Zipser & Lemone 1980; Giangrande et al. 2016), in some extreme cases the plumes can reach 20 km altitude with vertical up to $50\,m^{-1}$ (Dauhut et al. 2016). The difference in low-altitude vertical velocity with Sergeev et al. (2020) is due to a difference of shallow convection depth in the present study, allowing higher vertical velocity. This difference in tropopause height engenders a higher convective available potential energy and leads to higher vertical velocity. Above 17 km and up to 20 km, tropopause-overshooting convection is visible. For comparison, above the United States only approximately 2% of the overshooting convection reaches altitude 3 km above the tropopause (Cooney et al. 2018). In the absence of ozone heating in the model, the stratosphere lacks an inversion and is less stable, and could allow greater penetration. At 15 km, the vertical wind is dominated by the large cluster ($x = 75$; $y = 50$) km with a diameter of 50 km, but there are also several smaller plumes with a 10 km diameter. The deep convective plumes reaching their top altitude will engender upward and horizontally propagating gravity waves transporting heat and momentum. Such strong convective activity is known to affect Earth's atmosphere through the quasi-biennal oscillation (QBO) atmospheric feature (Dunkerton 1997). Convectively generated gravity waves are thought to take part in similar QBO-like features in giant-like and brown dwarf atmospheres (Showman et al. 2019).

This deep convection transports water vapor from 4 km up to the tropopause, leading to water condensation and thus cloud formation. Figure 4 shows a screenshot of a vertical cross section of the water clouds' abundance (top) and a vertical cross section of the water vapor enrichment (bottom), i.e., the relative change with regard to the mean water vapor vertical profile.

Between 12 (160 mbar) and 18 km, there is the presence of a complete cloud cover, as obtained in past GCM studies (Yang et al. 2013). The enrichment of water vapor at $x \sim 75$ km is related to the large vertical plumes visible in Figure 3(a), reaching up to 500% enhancement compared to the mean water vapor abundance at this same altitude. The maximum of this enrichment is above 20 km due to convection overshooting with a value as high as 10,000% The water is then advected horizontally by winds and visible between 200 and 250 km on the x-axis. On Earth, the water vapor enrichment at 100 hPa due to overshooting convection can reach up to 300% (Herman et al. 2017). Figure 5 shows the evolution with time of the stratospheric water vapor content (kilogram per kilogram of air). Soon after initialization, there is an abrupt decrease of water vapor due to the water vapor condensation, after the organization of convection the water vapor is transported by the large plume resulting to enrichment visible below 21 km with a maximum of increase by almost a factor 4 around 19 km. This water vapor advected by the convection from the lower atmosphere to the stratosphere is then advected by wind and can condense elsewhere on the planet. Between 21 and 23 km the atmosphere becomes drier.

Figure 6 displays the cloud fraction for the Proxima standard case. The equivalent of Earth stratocumulus clouds are visible below 5 km and covers about a tenth of the surface, compared to 20% for stratocumulus above the tropic ocean (Eastman et al. 2011). Between 12 and 19 km the cloud cover increases up to almost 100% as predicted by global climate modeling (Yang et al. 2013). Surface rain over the domain is equal to $15\,mm\,day^{-1}$. Under the deep convective plume, the surface rain reaches $120\,mm\,day^{-1}$.

The cloud cover is much lower in this CRM study compared to the GCM, especially for the low-altitude clouds, which greatly impact the radiation reaching the surface. The cloud fraction in the GCM is nonzero from the surface, with almost 60% to about 40% at 2 km, whereas for the CRM the cloud fraction is nonzero from 2 km, where the shallow convection ends. At this altitude the GCM cloud fraction is larger than 45%. This substantial discrepancy in cloud cover could explain the difference in albedo (discussed hereafter) between the CRM and GCM and shows the way to deal with the shallow convection. The high cloud layer is quite comparable in depth but at different altitude, 3 km higher for the CRM.

These clouds impact the fraction of shortwave radiation able to reach the surface but also the longwave infrared thermal emission. Figure 7(a) shows the outgoing longwave radiation (OLR) in brightness temperature units (Kelvins). The large cluster with a diameter of 150 km—where the OLR reaches a minimum value—corresponds to the vertical plume visible at $x \sim 75$ km, as shown in Figure 3(a). The brightness temperature drops to about 160 K in that structure, corresponding to an

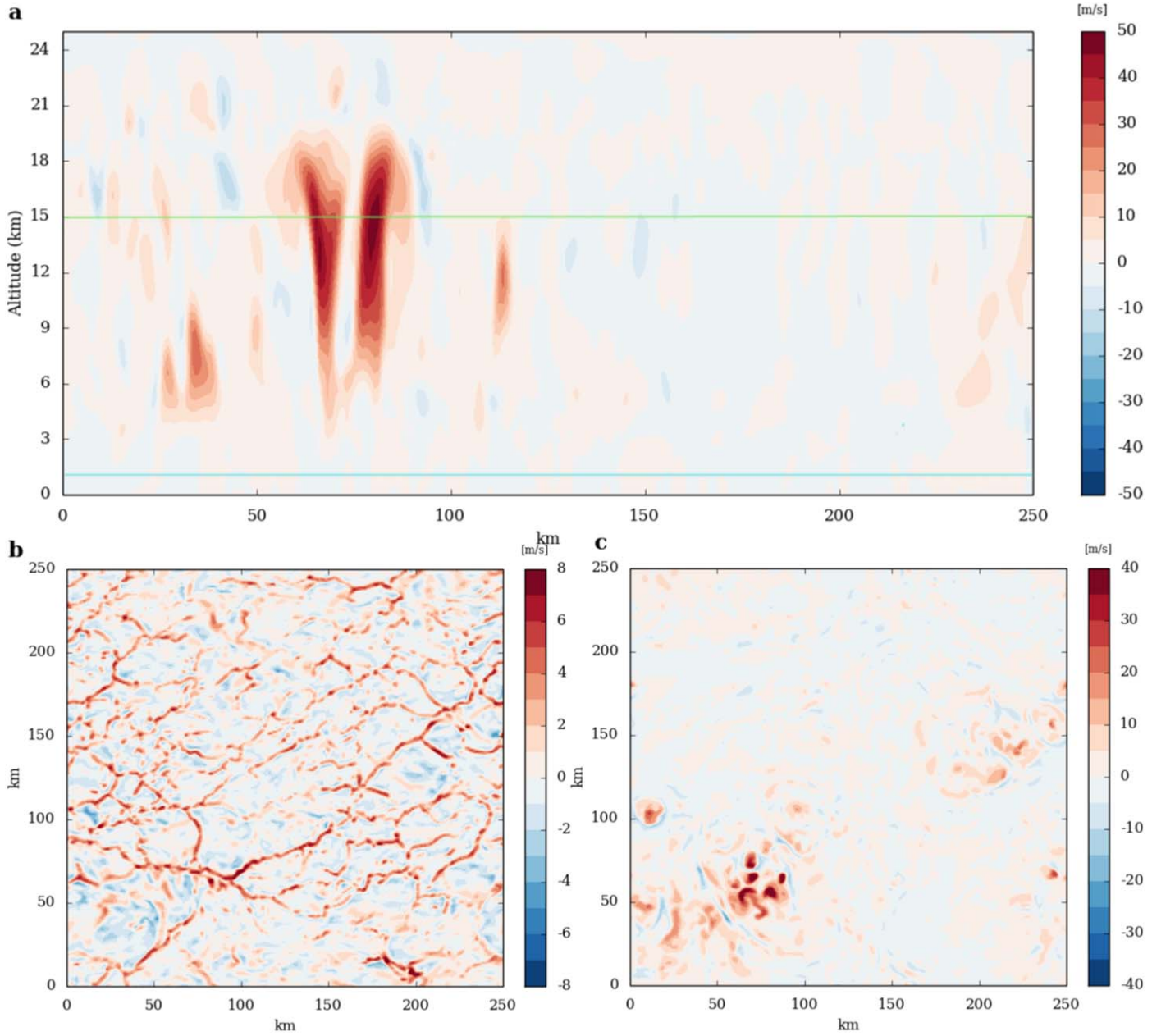

Figure 3. Screenshots after 30 hr of simulation of the vertical cross section (a) of the vertical wind (meter per second) and horizontal cross sections of the vertical wind (meter per second) at 1 km above the surface (b) and at 15 km above the surface (c) for the reference case. The cyan and green lines indicates the altitudes of the two horizontal cross sections, respectively, 1 and 15 km. The vertical cross section is at $y = 56$ km.

altitude of 16 km (Figure 2(a)). Outside of the cluster, the OLR can reach values up to 260 K, equivalent of an altitude of 6 km above the surface. This structure resemble convection aggregation (Wing & Emanuel 2014) but is transient, with a lifetime of about 3 hr, typical for a convective structure of that size (Roca et al. 2017). After it collapses, an other structure with similar size is emerging at a different location of the 250×250 km grid. Circular patterns of a few tens of kilometers are also visible. They are associated with the presence of smaller convective plumes. Figure 7(b) shows a horizontal cross section of the relative humidity at 8 km. The deep convective cluster is drying the non-convection area, acting like self-aggregation on Earth (Tobin et al. 2012).

Figure 7(c) shows the corresponding Bond albedo map and Figure 7(d) shows the corresponding vertically integrated water cloud (kilogram per square meter). Albedo can reach values from 0.05 in cloud-free regions up to 0.34 in the regions corresponding with the positions of high-altitude convective plumes, where there is the largest amount of clouds (reaching up to 5 kg m^{-2} in the column). The low-altitude stratocumulus clouds contribute for a significant part of the high albedo values as visible at $x = 160$ km with less than 1 Kg m^{-2} in the column. The domain-averaged value of the Bond albedo is 0.06, whereas the GCM Bond albedo is 0.32. This is explained first by the fact that the cloud coverage ($\sim$10%) for low-altitude stratocumulus clouds) is relatively low; and second by the fact that the cloud-free regions have a very low Bond albedo. The latter stems from the fact that the albedo of the ocean surface is low (0.07), that the Rayleigh scattering is inefficient around a cool star such as Proxima Centauri, and that the water vapor-

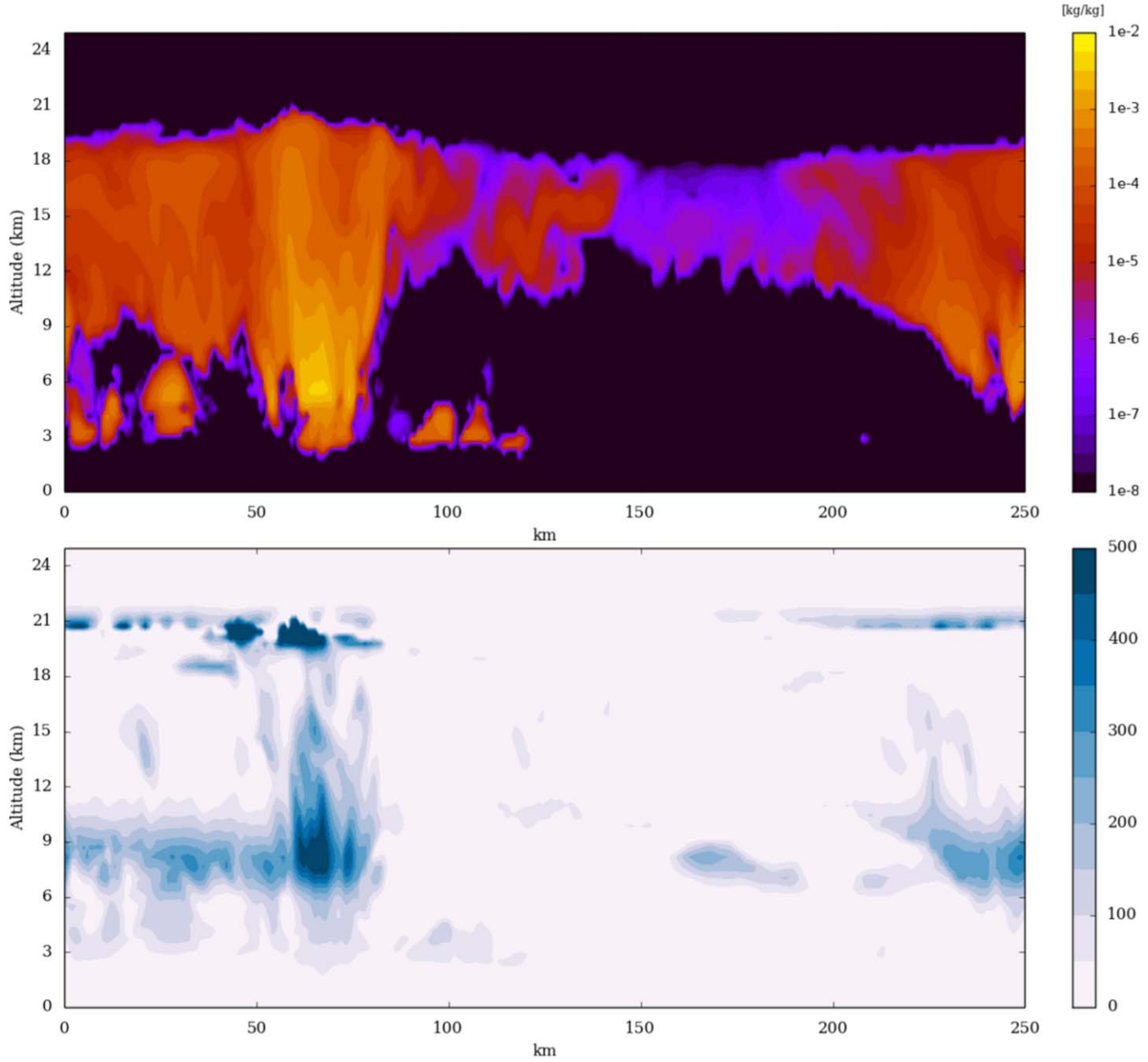

Figure 4. Screenshot of the the vertical cross section of the mixing ratio of water clouds (top panel) in kilogram per kilogram of air and of the water enrichment, i.e., the relative change in percentage) (bottom panel) for the reference case. For clarity, the scale of values enrichment is limited at 500% but it reach higher values. The vertical cross section is at $y = 56$ km.

enriched atmosphere absorbs efficiently near-infrared emission from the star. A similar reduction of the Bond albedo is also observed in the 1D cloud-free simulations of Kopparapu et al. (2013) (see Figure 6(a), calculated for a surface albedo of 0.3).

The maximum Bond albedo value in the CRM, corresponding to the large convective cluster, is comparable to the mean GCM Bond albedo at the substellar point. This substantial discrepancy could be explained by the significant difference in low-altitude clouds fraction between the CRM and GCM and difference in shallow convection. This value of albedo can be compared to the TOGA-COARE case with Sun spectra in the Appendix, where the albedo inside the deep convective plume is around 0.6, whereas the albedo is about 0.1 in the cloud-free region. The low value of the overall albedo is much smaller than previous GCM predictions (Yang et al. 2013, 2019b), which reflects the fact that outside deep convective layers where the albedo is close to previous GCM studies, the areas of low cloud fraction have low cloud albedo and therefore aggregation of convection, even transient like in the study, can have a strong effect on the overall albedo due to the low mass star spectra.

In addition to its synchronous rotation, another specificity of Proxima Centauri b compared to Earth is the spectra of its host star. Proxima Centauri is an M5.5 type star (Bessell 1991) with an effective temperature of 3050 K with a maximum of emission spectra of around 1 μm (Pavlenko et al. 2017). This shift toward the infrared is expected to impact the absorption of the stellar spectra by the atmosphere, especially by water.

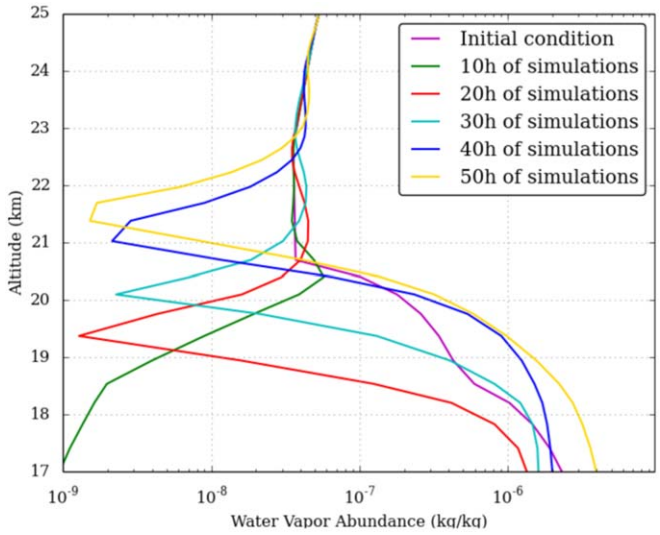

Figure 5. Vertical profile of domain-averaged water vapor content (kilogram per kilogram) in the stratosphere at initial condition, after 10, 20, 30, 40, and 50 hr of simulations for the reference case.

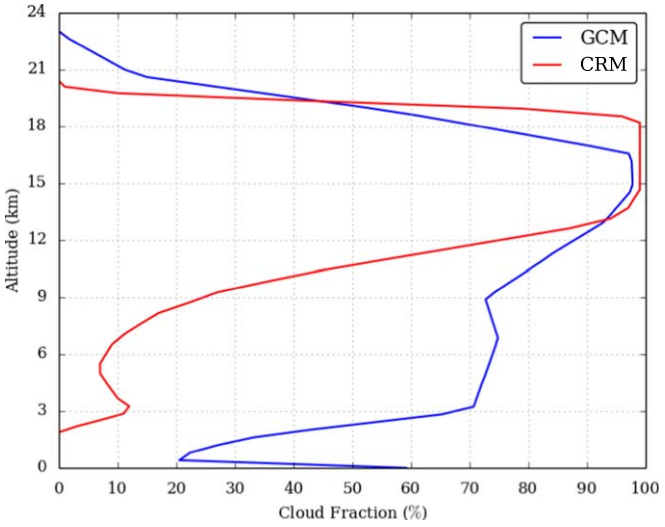

Figure 6. Comparison between the domain-averaged vertical profile of the cloud fraction obtained with the CRM (red) for the reference case and the time-averaged vertical profile of the cloud fraction from the LMD generic GCM (blue) at the chosen position (see Figure 1).

Figure 8 shows vertical profiles of the stellar heating (watt per square meter) for two water cloud features for both the TOGA-COARE case (blue line) with Sun spectra and the Proxima Centauri b reference case with M-star spectra (red line).

The two water cloud features displayed are high-altitude and low-altitude clouds and deep convection. As shown in the left panel, for Earth high clouds absorb solar heating around 1.5×10^2 hPa, while the absorption by the low-altitude clouds occurs at 6×10^2 hPa. For Proxima Centauri b, high clouds absorb solar heating between 2×10^2 hPa and 4 and 7×10^1 hPa with a maximum at 1×10^2 hPa and the absorption of the low-altitude clouds occurs at 5×10^2 hPa for the reference case. The shortwave heating by the low clouds on Proxima Centauri b is almost three times stronger than that of Earth, more efficiently shielding the surface from the incoming stellar radiation. For the deep convection case (right panel), for both Proxima Centauri b and Earth the shortwave heating is absorbing on a larger vertical scale, the heating is also stronger for Proxima Centauri b, more than three times that on Earth. A larger part of the energy coming from the host star is absorbed by the atmosphere gas and clouds, and therefore even with a lower overall albedo, the energy reaching the surface is lower for a planet orbiting an M-star than a Sun-like star (for an Earth-like atmosphere).

4. Impact of the Incident Flux

Figure 9 shows a comparison of the cloud coverage for the reference case with the FAST-1080 and FAST-1280 cases (all with an 11 day rotation period). In all the three cases, there is a high-altitude cloud layer. The altitude of this layer is determined by the thermal structure. The tropopause increases with the stellar flux, with a value of 17 km (50 hPa) for the standard case, 19 km (32 hPa) for the FAST-1080 case, and 21 km (20 hPa) for the FAST-1280 case (see Figure 2(a)). The thickness of this high-altitude cloud layer decreases with the increase in the incident flux. This inverted trend is due to the low-altitude clouds. The increasing stellar flux engenders a thicker shallow convection, from around 3.0 km for the reference case to 5.6 km for the FAST-1280 case, leading to more extended vertical mixing of the water vapor in the shallow convection. The domain-averaged value for the standard case is 8×10^{-3} kg kg^{-1}, 1.1×10^{-2} kg kg^{-1} for the FAST-1080 case, and 2.3×10^{-2} kg kg^{-1} for the FAST-1280 case. This increase in water vapor by the shallow convection triggers more condensation, leading to an increase of the low-altitude clouds' coverage, reaching up to 60% for the FAST-1280 case.

Figure 10 shows the atmospheric albedo (left) and the OLR brightness temperature (Kelvin) for the reference case (top), FAST-1080 case (middle), and FAST-1280 case (bottom). One noticeable behavior is the increase of both the atmospheric albedo and the OLR with the increase of the stellar flux. The structure of the albedo map for the standard case is dominated by the high cloud layer visible in the OLR map. For the FAST-1080 case, the contribution of high-altitude clouds is visible in the center of the map but the low-altitude cloud layer is dominating with small patchy structures. The contribution of low-altitude clouds is even more important for the FAST-1280 case where the contribution of the high-altitude clouds, visible on the OLR map, is barely noticeable.

With the increase in the stellar flux, the thermal structure of the atmosphere changes with an increase in the tropopause height as well as an increase in the atmospheric water vapor mixing ratio. This increase of stellar flux induces a thicker shallow convection leading to an increase of the low-altitude cloud layer coverage. This increase of the low-altitude clouds engender an increase of the atmospheric albedo and a stronger shortwave cloud radiative feedback. This temperature trend is consistent with anvil cloud fraction SST dependence on Earth (Bony et al. 2016), where an increase of the SST reduces the cloud fraction.

Simulations with an initial surface temperature of around 350 K, corresponding to incoming stellar flux of 1500 and 1610 W m m^{-1} for the fast and slow cases, respectively, were conducted but not shown here. The abundance of water vapor in the atmosphere reaches values superior to 20%, going over the dilute regime, therefore a condensation of water vapor would lead to a significant pressure change not taken into account by the model. To be able to study such temperature

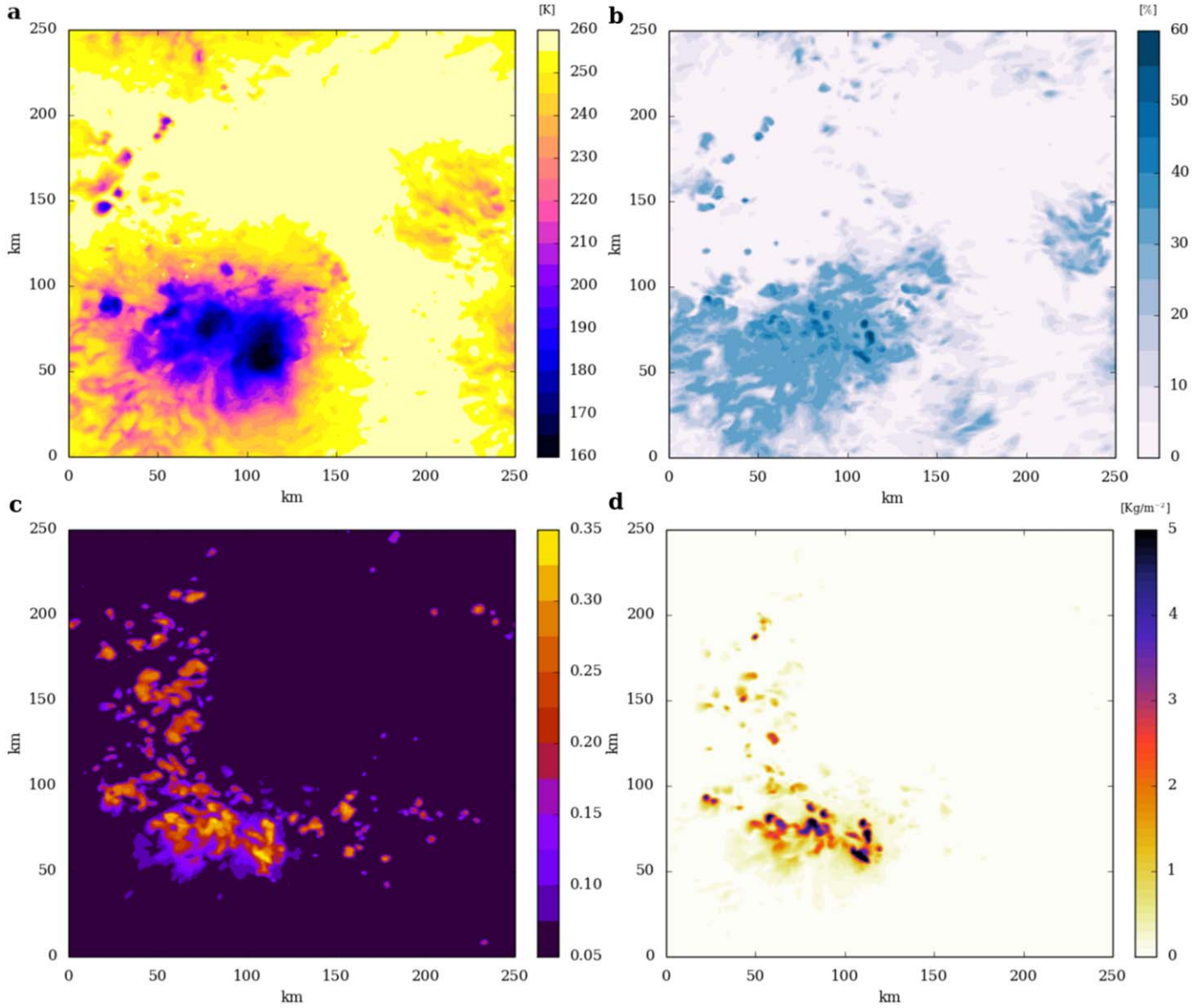

Figure 7. Screenshot of the OLR brightness temperature in Kelvin (a), the relative humidity at 8 km (b), the Bond albedo (c), and vertically integrated water clouds abundance in kilogram per square meter (d) for an incident stellar flux of 880 W m^{-2} and an 11 day rotation period.

ranges, changes need to be carried out to take into account the non-dilute regime.

5. Impact of the Rotation Period

The rotation period has an important impact on the circulation of a planetary atmosphere. The strength of the Coriolis force dictates the extend of the thermally direct latitudinal circulations and the surface temperature distribution, which drives atmospheric circulation (Pierrehumbert 2010). From Figure 2(a), wit can be seen that the thermal structures and water vapor vertical distributions are similar for the slow and fast rotation cases (for a given surface temperature), whereas the advection heating rates have different behavior (Figure 2(b)). For the slow cases, the profile of advection heating rates for the three cases of solar insolation have similar behavior with positive values region between 12 and 18 km and above a strong negative value region between 16 and 21 km. On the other hand, for the fast cases the advection heating rates are only negative below 21 km.

Figure 11 shows the comparison of the cloud coverage for the six cases studied in our work: the reference case, FAST-1080 and FAST-1280 with an 11 day rotation period and SLOW-800, SLOW-1000, and FAST-1250 with a 60 day rotation period. The height of the tropopause is very similar for the two rotation periods but the advection heating rates are quite different with stronger values for the 60 day rotation rate. For the six cases, there is a high-altitude cloud layer thinner with increasing stellar flux as described in the previous section. The depth of this cloud layer also increases with the rotation rate. The high-altitude cloud layer is about 1.5 km thicker for the SLOW-800 case compared to the reference case, 2 km thicker for the SLOW-1000 case compared to the FAST-1080 case. For the SLOW-1250 case, this layer is not only thicker but it reaches higher cloud fraction values. The low-altitude cloud coverage is very similar for the four highest incident stellar flux cases, whereas for the two lowest there is a

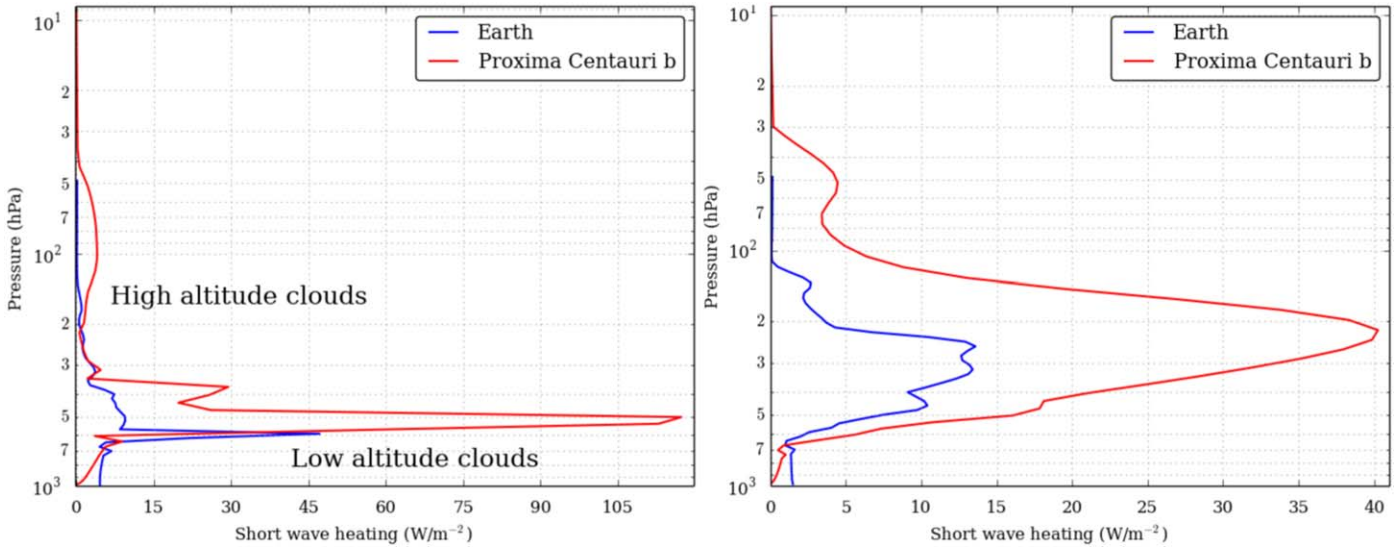

Figure 8. Vertical profiles of incident stellar heating (in watt per square meter, per atmospheric layer). The red lines are for the Proxima Centauri b reference case and the blue lines are for the TOGA-COARE case. The left panel is for the case of the presence of both high-altitude clouds and low-altitude clouds and the right panel is for the case of deep convection.

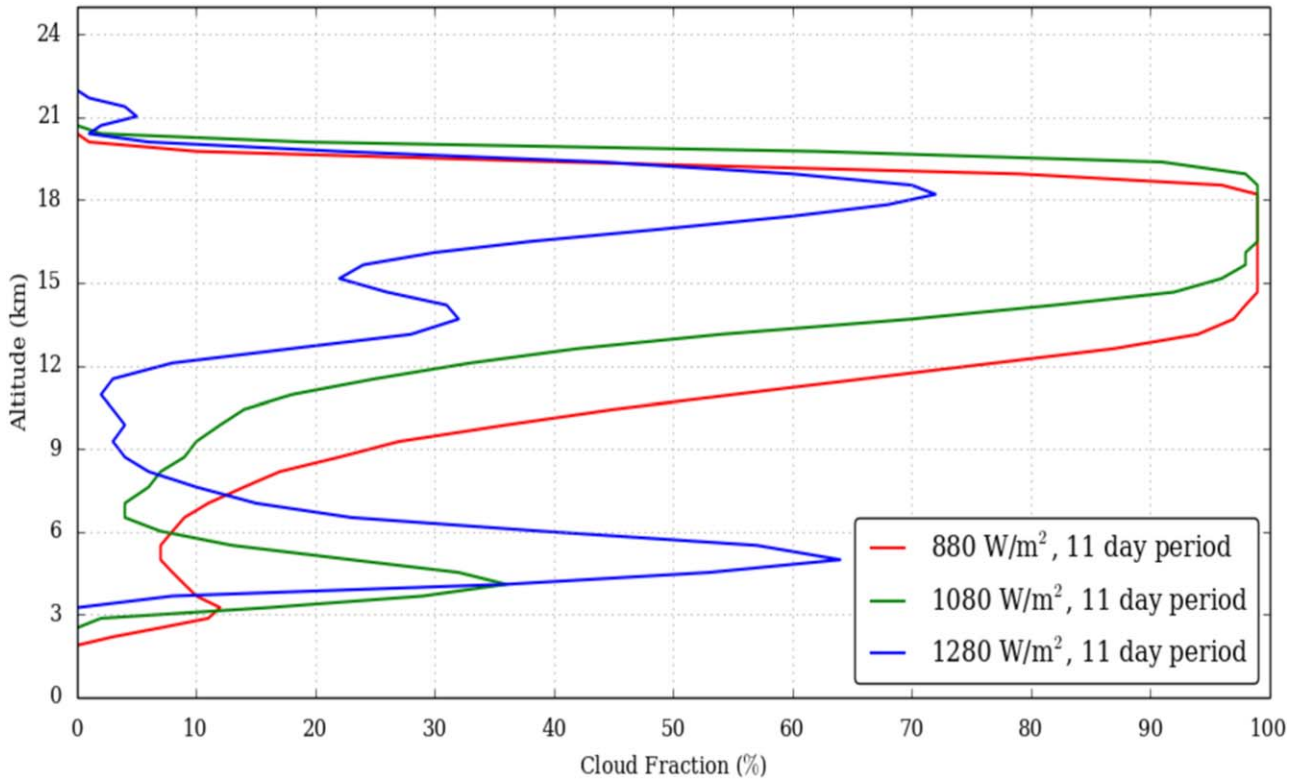

Figure 9. Comparison of the domain-averaged cloud fraction for the reference case (top), FAST-1080 (middle), and FAST-1280 (bottom) cases.

significant difference with the rotation period. The low-altitude cloud coverage of the SLOW-800 case is almost four times the coverage of the reference case. The altitude of the lower cloud deck is varying with the incident flux but also with the rotation period. For the 60 day cases, the top of the shallow convective layer is lower, especially at high stellar flux. This effect increases the albedo and can be attributed to the thicker high-altitude cloud layer absorbing and reflecting more incident stellar flux.

Figure 12 shows the albedo (left) and the OLR brightness temperature for the SLOW-1000 (top), SLOW-1000 (middle), and SLOW-1250 (bottom) cases. Compared to Figure 10, the OLR brightness temperature is lower for the 60 day rotation period than for the similar 11 day rotation case. For example, the large-scale structure visible in the Figure 12 (bottom right) for the SLOW-1250 has a stronger OLR flux, i.e., a smaller brightness temperature, than the large-scale structure visible in the Figure 10 (bottom right panel) for the FAST-1280 case. This is due to the fact that the high-altitude clouds is more

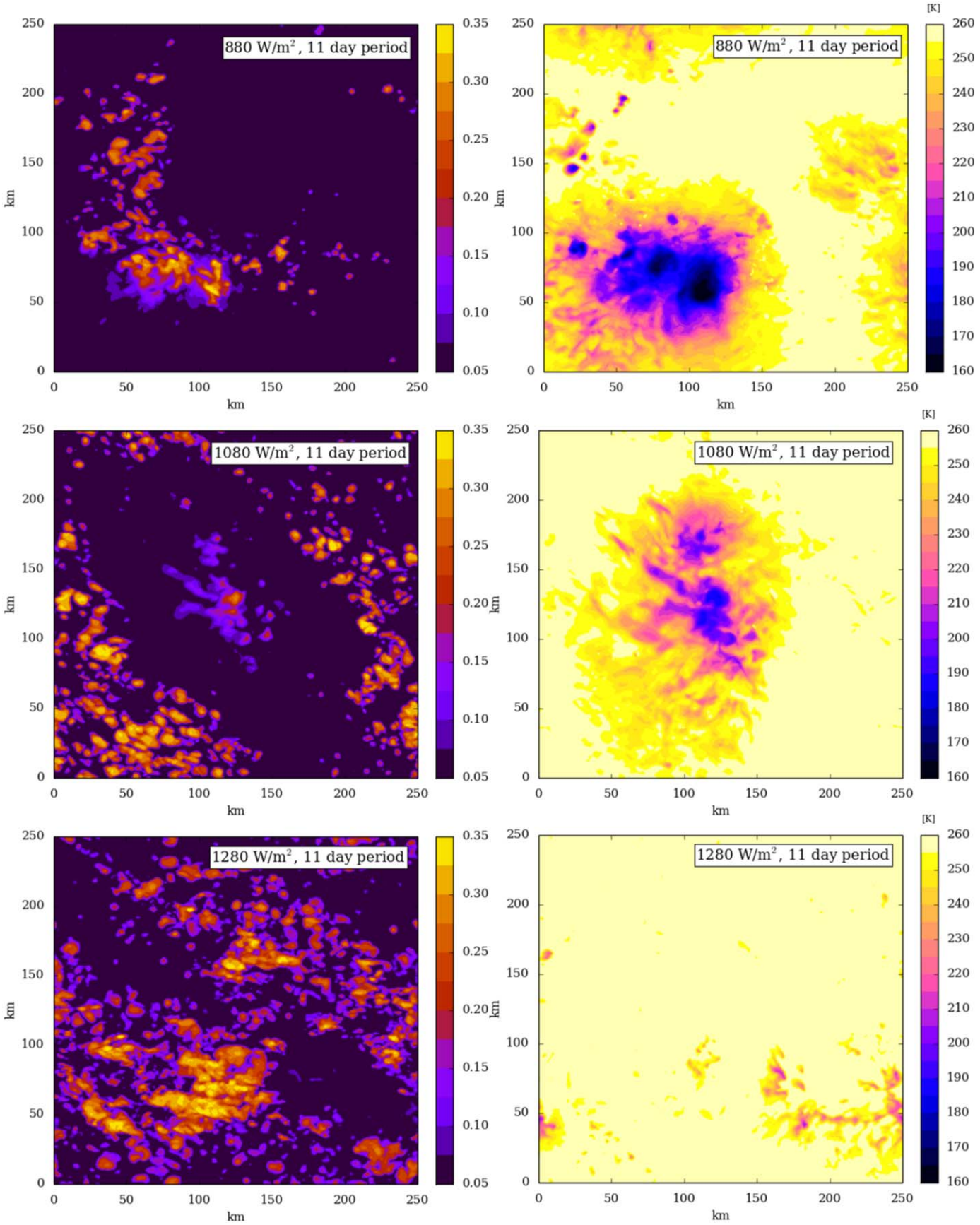

Figure 10. Snapshots of albedo (left panels) and OLR brightness temperature in Kelvin (right panels) for Proxima b (top panels), FAST-1080 (middle panels), and FAST-1280 (bottom panels) cases.

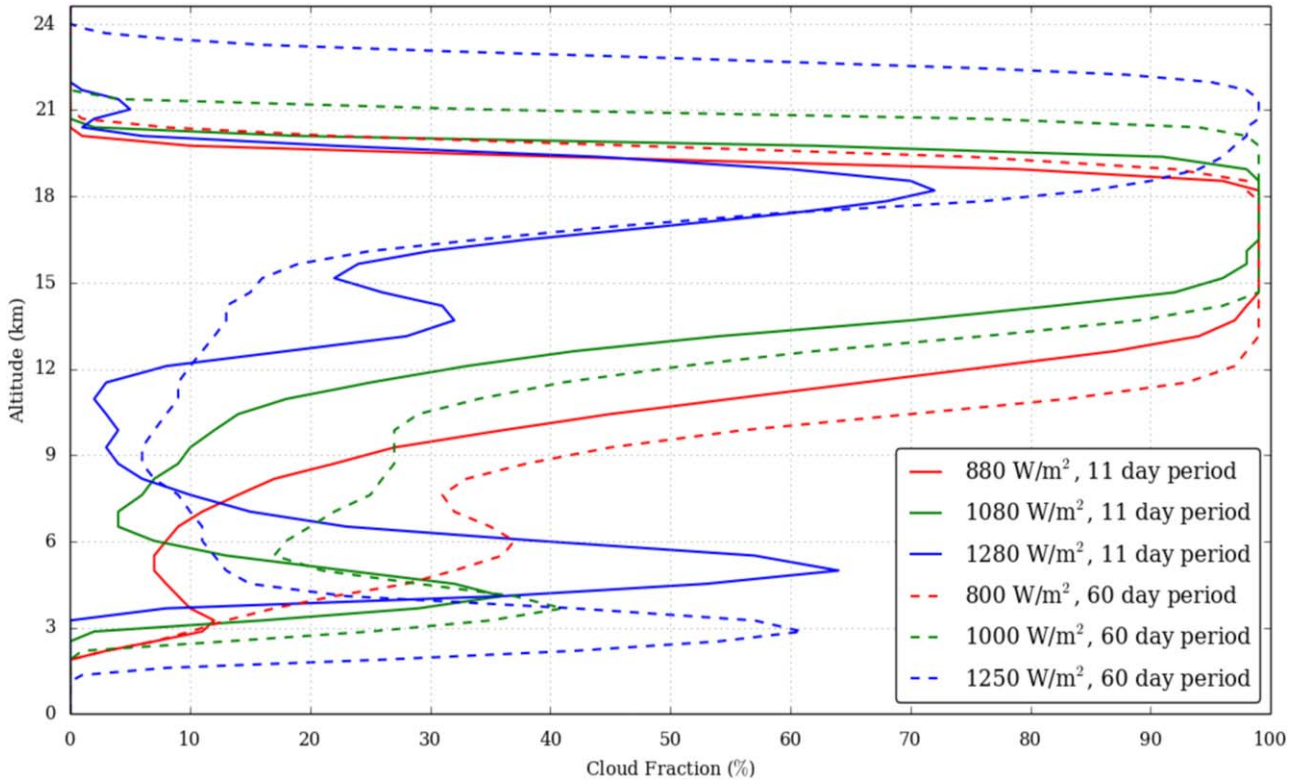

Figure 11. Comparison of the domain-averaged cloud fraction for the SLOW-800 (top), SLOW-1000 (middle), and SLOW-1250 (bottom) cases.

developed for the 60 day rotation period and that the updrafts are stronger. The increase of low clouds albedo with the increase of surface temperature is also as noticeable with the 60 day rotation rate as it is for the 11 day rate.

In summary, the increase in the rotation period engenders a change in the circulation regime leading to a different behavior of the advection heating rate in altitude. This increase of the high-altitude cloud layer thickness is linked to the vertical structure of the profile of advection heating rates between 12 and 21 km. This structure with positive values followed by negative heating rates will trigger additional convective activity in this region. The increased thickness of the altitude cloud layer corresponds to the region where this triggering takes place, between 12 and 19 km for the SLOW-800 case, 15–20 km for the SLOW-1000 case, and 18–24 km for the SLOW-1250 case. This triggering will increase the convective activity and the vertical transport of water vapor in this region, and therefore engender a thicker cloud layer. With this change in high-altitude clouds, a decrease in shallow convective layer is occurring leading to an increase of the Bond albedo and cloud feedback.

6. Discussion

Figure 13 shows a comparison of the domain-averaged Bond albedo for the six cases as a function of the incident stellar flux. The trends discussed in Sections 4 and 5 are visible. The Bond albedo shows an increase of about 20% with the increasing flux and an increase of between 5% and 10% with increasing rotation period. The study of Yang et al. (2013) found a similar trend in the increase of Bond albedo with insolation: between stellar fluxes of 1000 and 1200 W m^2, the Bond albedo increases by 7%, although with much higher values around 0.45. Using a GCM with a high-resolution zoom in the substellar region, Sergeev et al. (2020) studied the convection on tidally locked Earth-like planets. A notable discrepancy is the fact that the albedo inside the high-resolution area is higher than with the low-resolution GCM in Sergeev et al. (2020), whereas in this study the albedo of the CRM is lower than in the GCM. The main noticeable difference between the two models is that in Sergeev et al. (2020), the large-scale forcing is given by the GCM fields (temperature, water content, winds,...) in real time, whereas in this study the large-scale forcing is represented by a single time-averaged vertical profile in temperature fixed in time and space. This difference in handling the large-scale forcing could lead to a difference in the shallow convection depth and therefore a difference in albedo. The aggregation of convection shown in Section 3, and not seen in the Sergeev et al. (2020) study, is also one factor of this albedo discrepancy. These differences between the two models call for more global climate modeling in such an atmospheric environment leading to an intercomparison, possibly in the same way as the TRAPPIST-1 Habitable Atmosphere Intercomparison GCM for exoplanets (Fauchez et al. 2020) was carried out, in order to improve the understanding of convection processes in exoplanetary environments.

The model does not calculate the difference between a liquid water cloud and a water ice cloud. The impact of the general circulation is represented in the model by a constant heating rate profile, and a water vapor tendency profile could be imposed to the domain to take into account the water vapor advection near the substellar point. The impact of the temperature of the general circulation is represented with a constant tendency profile close to the surface, and a more realistic approach with a time-dependent profile could improve the physical representation of the advection near the substellar

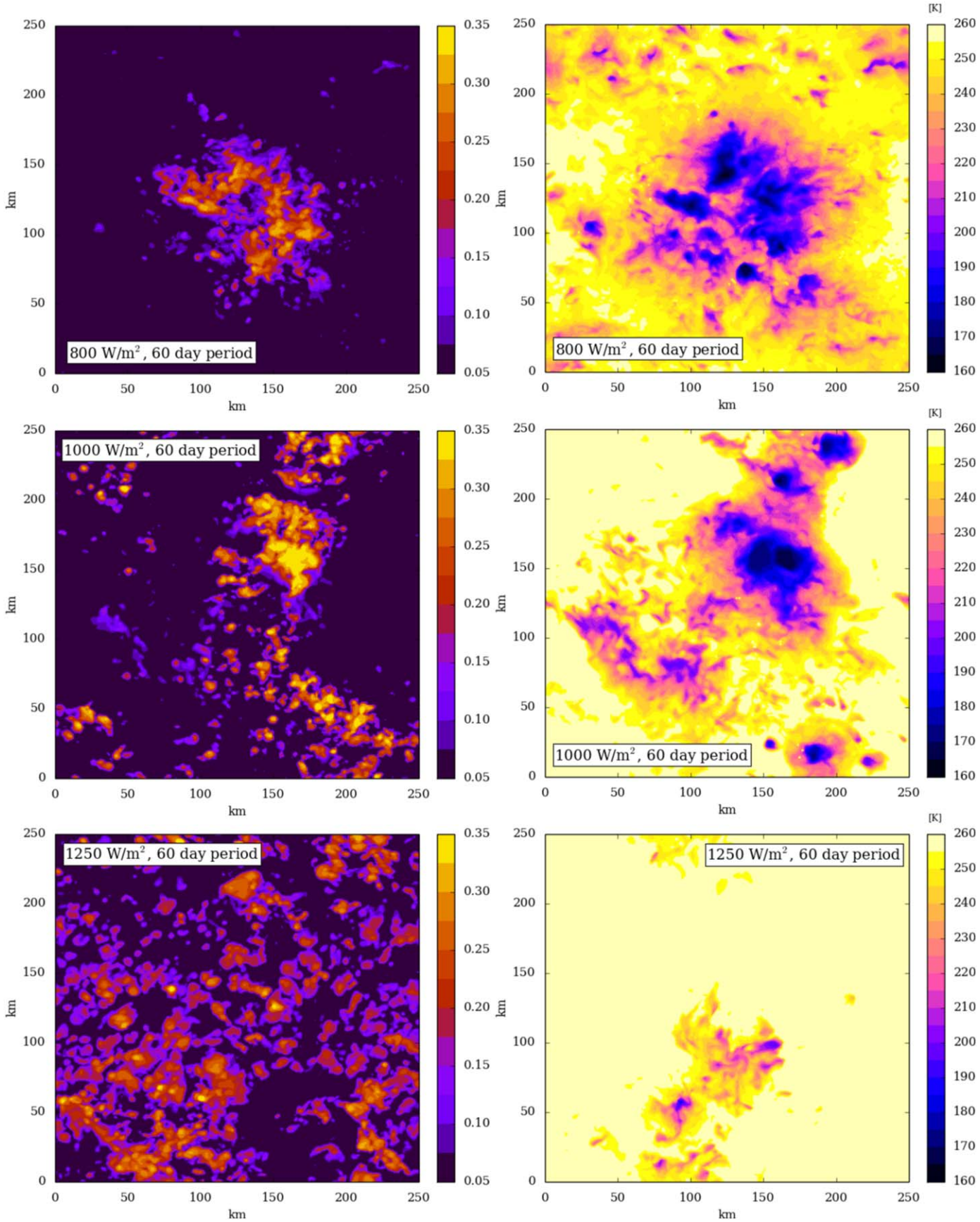

Figure 12. Snapshots of albedo (left panels) and OLR brightness temperature in Kelvin (right panels) for the SLOW-800 (top panels), SLOW-1000 (middle panels), and SLOW-1250 (bottom panels) cases.

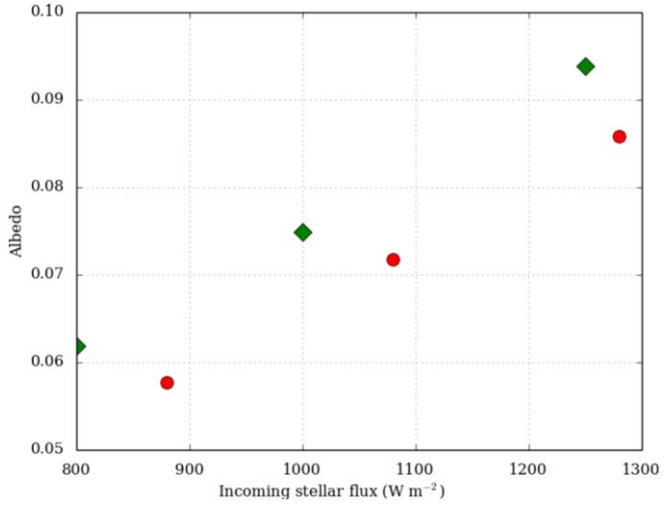

Figure 13. Domain-averaged Bond albedo as a function of the incident stellar flux (in watt per meter) for the CRM. Diamonds are for slow cases and circles for the fast cases.

point. Another improvement in the model would be to take into account ocean circulation. Del Genio et al. (2019) showed the impact of such circulation on the SST and the clouds' self-aggregation (Müller & Hohenegger 2020) and how SST anomalies can favor the aggregation of convection (Shamekh et al. 2020). The oceanic circulation is also believed to have a significant impact on atmospheric circulation, with a planetary heat transport dominated by the ocean at moderate incident stellar fluxes and by the atmosphere near the inner edge of the HZ (Yang et al. 2019a). This is assuming an oceanic surface, in which case, a simulation of an continental surface also needs to be carried out.

7. Conclusion

We presented the LMD generic CRM coupled to realistic radiative transfer and a non-Earth-based cloud microphysics model. This versatile model is able to resolve realistic Earth's tropical convection as well as to perform in extreme insolation conditions such as those experienced on tidally locked planetary atmospheres such as Proxima b. In this study, we presented the results of resolved convection simulations of the Proxima b environment, assuming an Earth-like atmospheric composition, for several incident stellar fluxes and rotation periods.

For the standard case, organized convection is resolved with a shallow convection of 2.5 km in depth and 60 km in diameter. Convective clouds are present reaching up to 20 km in altitude and 150 km in diameter. Inside this strong updraft, vertical velocity can reach 40 m s^{-1}, with surface rain values of 120 mm day^{-1} under. A thick 100% cloud cover between 12 and 18 km is present. The convective clouds transport water vapor from the surface to the troposphere. Around 19 km, this enrichment of water vapor is maximal with a four-fold increase compared to initial conditions.

Simulations with higher stellar fluxes and slower rotation rates were conducted. The Bond albedo is sensitive to these two physical parameters. The albedo increases when the stellar flux increases, from an increase in the low-altitude cloud fraction and a decrease in the depth of the high-altitude cloud layer, overall increasing the albedo. The decrease in the rotation rate has the effect of changing the general circulation, especially between 20 and 30 km. This difference in circulation triggers a thicker high-altitude cloud layer thus increasing the Bond albedo.

The shortwave cloud feedback resolved by the model is lower than the cloud feedback predicted by previous GCM simulations (Yang et al. 2013, 2019b). The shallow convection and low-altitude clouds are different in the two models, in the CRM the shallow convection is thicker and the cloud coverage of low-altitude clouds is lower leading to a smaller albedo. The high-altitude cloud coverage is similar between the two models. While the CRM exhibits a small overestimation of the shallow convection height, this discrepancy between the cloud coverage obtained with this model and the cloud coverage from the LMD GCM suggests that the moist convection parameterization scheme does not correctly handle the convection and cloud formation of the near surface area. This study will be used to calibrate a more realistic convection representation such as a thermal plume model (Rio & Hourdin 2008; Rio et al. 2010).

The simulations show signs of organized convection with a cellular cluster of about 150 km in diameter. However the domain size could be one limit to the aggregation of convection. In such an incoming stellar environment, it is important to consider the albedo effect of aggregation of convection. Simulations with a larger horizontal domain should be performed to fully understand the mechanisms of that phenomenon (Wing & Emanuel 2014; Bretherton & Khairoutdinov 2015).

The high velocity inside the largest convective clouds with water cycle is the perfect environment for the occurrence of lightning. NOx and HOx chemistry could therefore be triggered and have an impact on stellar absorption (Ardaseva et al. 2017) and on the HCN production rate, a key feedstock of life's building blocks (Rimmer & Rugheimer 2019). To investigate these effects, improvement is needed in the representation of the water cycle in the microphysical model, which would need to separately handle liquid water cloud and ice water cloud as well as the inclusion of graupel.

The simulations here are for an atmospheric composition close to the Earth. Thanks to the versatility of the model, the impact of different compositions of the cloud coverage will be explored; for example, the impact of CO_2 abundance, thought to decrease stratocumulus cloud coverage (Schneider et al. 2019). Water vapor has been detected on the HZ super-Earth exoplanet K2-18 b in an atmosphere thought to be hydrogen-rich (Benneke et al. 2019; Tsiaras et al. 2019). The difference in molecular mass between hydrogen and water will engender compositional buoyancy that will impact the convection (Leconte et al. 2017; Charnay et al. 2021). Another compositional effect that will be explored is the non-dilute convection regime (Ding & Pierrehumbert 2016), where the condensing component is the principal or non-negligible species.

The authors thank the anonymous reviewer, who helped improve the paper. The authors thank Caroline Muller and Aymeric Spiga for helpful comments and discussions. This project has received funding from the European Research Council (ERC) under the European Union's Horizon 2020 research and innovation program (grant agreement No. 740963/EXOCONDENSE). This project has received funding from the European Union's Horizon 2020 research and innovation program under the Marie Sklodowska-Curie grant agreement No. 832738/ESCAPE. This work was granted

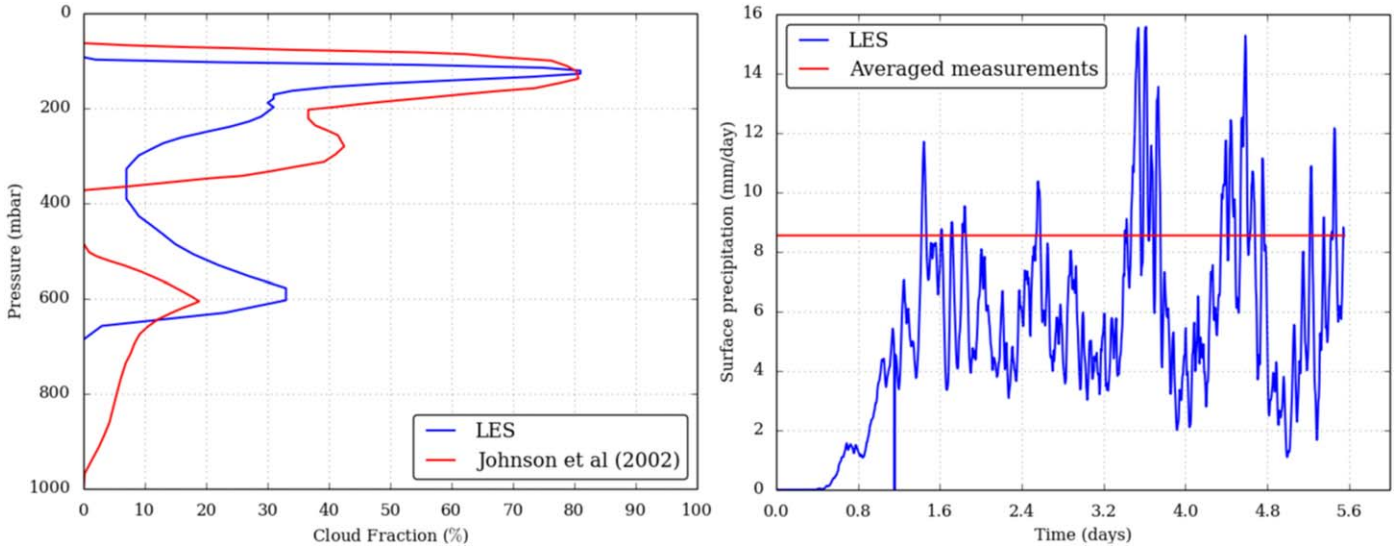

Figure 14. Left panel: average cloud fraction resolved by the model (CRM) and by Johnson et al. (2002). Right panel: surface rain (millimeters per day) over the whole domain (CRM) and averaged measurements.

access to the High-Performance Computing (HPC) resources of the Centre Informatique National de l'Enseignement Supérieur (CINES) under the allocations no A0020101167 and A0040110391 made by Grand Équipement National de Calcul Intensif (GENCI). This work was granted access to the HPC resources of the Institute for Computing and Data Sciences (ISCD) at Sorbonne Université. This work benefited from the IPSL ciclad-ng facility. M.T. thanks the Gruber Foundation for its generous support of this research. This work has been carried out within the framework of the National Centre of Competence in Research Planets supported by the Swiss National Science Foundation. M.T. acknowledges the financial support of the SNSF.

Appendix
TOGA-COARE Modeling

As stated in Section 2, the model presented in this study was tested with Earth's tropical convection data from the TOGA-COARE campaign. The temperature, pressure, water vapor, and wind profiles are taken from the measurement campaign. Advection heating and water vapor advection are also taken into account. The surface temperature is set up at the beginning of the simulations and then is free to evolve during the simulation. With similar settings as those described in Section 2 with a Sun spectrum and a diurnal cycle, the model resolves convection, as shown in Figure 14, after 6 Earth days of simulation.

The cloud fraction (left) is calculated using Xu & Krueger (1991) formulations to be compared to those of Johnson et al. (2002). The overall behavior is very similar, however, the low-altitude clouds are slightly overestimated by the model and the high-altitude clouds are a little underestimated. The height of the cloud bottom boundary, about 750 hPa, is also over-estimated compared to similar modeling, by about 950 hPa (Daleu et al. 2015). The surface rain resolved by the model is close to the average of the models from Johnson et al. (2002) and Wang et al. (2013). However, the model is not designed to reproduce extreme events, such as a strong sudden increase in domain-averaged surface rain over 40 mm day^{-1} (Wang et al. 2013). This model is suited to realistically exhibit Earth's convective behavior in the tropics.

ORCID iDs

Maxence Lefèvre https://orcid.org/0000-0002-3143-9716
Martin Turbet https://orcid.org/0000-0003-2260-9856
Raymond Pierrehumbert https://orcid.org/0000-0002-5887-1197

References

Anglada-Escudé, G., Amado, P. J., Barnes, J., Berdiñas, Z. M., & Butler 2016, Natur, 536, 437
Ardaseva, A., Rimmer, P. B., Waldmann, I., et al. 2017, MNRAS, 470, 187
Atkinson, B. W., & Wu Zhang, J. 1996, RvGeo, 34, 403
Auclair-Desrotour, P., Leconte, J., & Mergny, C. 2019, A&A, 624, A17
Benneke, B., Wong, I., Piaulet, C., et al. 2019, ApJ, 887, L14
Bessell, M. S. 1991, AJ, 101, 662
Bolmont, E., Libert, A.-S., Leconte, J., & Selsis, F. 2016, A&A, 591, A106
Bonfils, X., Astudillo-Defru, N., Díaz, R., et al. 2018, A&A, 613, A25
Bony, S., Stevens, B., Coppin, D., et al. 2016, PNAS, 113, 8927
Boucher, O., Le Treut, H., & Baker, M. B. 1995, JGRD, 100, 16
Bretherton, C. S., & Khairoutdinov, M. F. 2015, JAMES, 7, 1765
Charnay, B., Blain, D., Bézard, B., et al. 2021, A&A, 646, A171
Charnay, B., Forget, F., Wordsworth, R., et al. 2013, JGRD, 118, 10414
Charnay, B., Meadows, V., & Leconte, J. 2015a, ApJ, 813, 15
Charnay, B., Meadows, V., Misra, A., Leconte, J., & Arney, G. 2015b, ApJL, 813, L1
Cooney, J. W., Bowman, K. P., Homeyer, C. R., & Fenske, T. M. 2018, JGRD, 123, 329
Daleu, C. L., Plant, R. S., Woolnough, S. J., et al. 2015, JAMES, 7, 1576
Dauhut, T., Chaboureau, J.-P., Escobar, J., & Mascart, P. 2016, JAtS, 73, 5041
Deardorff, J. W. 1972, JAtS, 29, 91
Del Genio, A. D., Way, M. J., Amundsen, D. S., et al. 2019, AsBio, 19, 99
Ding, F., & Pierrehumbert, R. T. 2016, ApJ, 822, 24
Dunkerton, T. J. 1997, JGR, 102, 26053
Eastman, R., Warren, S. G., & Hahn, C. J. 2011, JCli, 24, 5914
Edson, A., Lee, S., Bannon, P., Kasting, J. F., & Pollard, D. 2011, Icar, 212, 1
Eymet, V., Coustet, C., & Piaud, B. 2016, J. Phys. Conf. Ser., 676, 012005
Fauchez, T., Turbet, M., Wolf, E. T., et al. 2020, GMDD, 13, 707
Forget, F., Wordsworth, R., Millour, E., et al. 2013, Icar, 222, 81
Giangrande, S. E., Toto, T., Jensen, M. P., et al. 2016, JGRD, 121, 12,891
Gillon, M., Triaud, A. H. M. J., Demory, B.-O., et al. 2017, Natur, 542, 456
Grabowski, W. W. 2001, JAtS, 58, 978
Grabowski, W. W., & Moncrieff, M. W. 2002, QJRMS, 128, 2349
Hammond, M., & Pierrehumbert, R. T. 2018, ApJ, 869, 65

Haqq-Misra, J., Wolf, E. T., Joshi, M., Zhang, X., & Kopparapu, R. K. 2018, ApJ, 852, 67
Held, I. M., Hemler, R. S., & Ramaswamy, V. 1993, JAtS, 50, 3909
Herman, R. L., Ray, E. A., Rosenlof, K. H., et al. 2017, ACP, 17, 6113
Johnson, D. E., Tao, W.-K., Simpson, J., & Sui, C.-H. 2002, JAtS, 59, 3492
Kasting, J. F., Whitmire, D. P., & Reynolds, R. T. 1993, Icar, 101, 108
Kikuchi, K., & Wang, B. 2008, JCli, 21, 2680
Kirkpatrick, J. D., Gelino, C. R., Cushing, M. C., et al. 2012, ApJ, 753, 156
Klemp, J. B., Dudhia, J., & Hassiotis, A. D. 2008, MWRv, 136, 3987
Kopparapu, R. K., Ramirez, R., Kasting, J. F., et al. 2013, ApJ, 765, 131
Kopparapu, R. k., Wolf, E. T., Haqq-Misra, J., et al. 2016, ApJ, 819, 84
Leconte, J., Forget, F., Charnay, B., et al. 2013a, A&A, 554, A69
Leconte, J., Forget, F., Charnay, B., Wordsworth, R., & Pottier, A. 2013b, Natur, 504, 268
Leconte, J., Selsis, F., Hersant, F., & Guillot, T. 2017, A&A, 598, A98
Lefèvre, M., Lebonnois, S., & Spiga, A. 2018, JGRE, 123, 2773
Lefèvre, M., Spiga, A., & Lebonnois, S. 2017, JGRE, 122, 134
Lefèvre, M., Spiga, A., & Lebonnois, S. 2020, Icar, 335, 113376
Lilly, D. K. 1962, Tell, 14, 148
Lipps, F. B., & Hemler, R. S. 1986, JAtS, 43, 1796
Lipps, F. B., & Hemler, R. S. 1988, JAtS, 45, 2428
Lovis, C., Snellen, I., Mouillet, D., et al. 2017, A&A, 599, A16
Moeng, C., Dudhia, J., Klemp, J., & Sullivan, P. 2007, MWRv, 135, 2295
Muller, C. J., & Held, I. M. 2012, JAtS, 69, 2551
Müller, S. K., & Hohenegger, C. 2020, JAMES, 12, e2019MS001698
Pavlenko, Y., Suárez Mascareño, A., Rebolo, R., et al. 2017, A&A, 606, A49
Pierrehumbert, R. T. 1995, JAtS, 52, 1784
Pierrehumbert, R. T. 2010, Principles of Planetary Climate (Cambridge: Cambridge Univ. Press)
Rajpurohit, A. S., Reylé, C., Allard, F., et al. 2013, A&A, 556, A15
Rimmer, P. B., & Rugheimer, S. 2019, Icar, 329, 124
Rio, C., & Hourdin, F. 2008, JAtS, 65, 407
Rio, C., Hourdin, F., Couvreux, F., & Jam, A. 2010, BoLMe, 135, 469
Roca, R., Fiolleau, T., & Bouniol, D. 2017, JCli, 30, 4283
Rossow, W. B. 1978, Icar, 36, 1
Schneider, T., Kaul, C. M., & Pressel, K. G. 2019, NatGe, 12, 163
Schumacher, C., Stevenson, S. N., & Williams, C. R. 2015, QJRMS, 141, 2277
Sergeev, D. E., Lambert, F. H., Mayne, N. J., et al. 2020, ApJ, 894, 84
Shamekh, S., Muller, C., Duvel, J.-P., & D'Andrea, F. 2020, JAtS, 77, 3733
Showman, A. P., & Polvani, L. M. 2011, ApJ, 738, 71
Showman, A. P., Tan, X., & Zhang, X. 2019, ApJ, 883, 4
Skamarock, W. C., & Klemp, J. B. 2008, JCoPh, 227, 3465
Spiga, A., Barth, E., Gu, Z., et al. 2016, SSRv, 203, 245
Spiga, A., & Forget, F. 2009, JGRE, 114, E02009
Spiga, A., Forget, F., Lewis, S. R., & Hinson, D. P. 2010, QJRMS, 136, 414
Spiga, A., Guerlet, S., Millour, E., et al. 2020, Icar, 335, 113377
Stubenrauch, C. J., Chédin, A., Rädel, G., Scott, N. A., & Serrar, S. 2006, JCli, 19, 5531
Sullivan, P. P., & Patton, E. G. 2011, JAtS, 68, 2395
Tobin, I., Bony, S., Holloway, C. E., et al. 2013, JAMES, 5, 692
Tobin, I., Bony, S., & Roca, R. 2012, JCli, 25, 6885
Tompkins, A. M. 2001, JAtS, 58, 529
Tsiaras, A., Waldmann, I. P., Tinetti, G., Tennyson, J., & Yurchenko, S. N. 2019, NatAs, 3, 1086
Tuomi, M., Jones, H. R. A., Butler, R. P., et al. 2019, arXiv:1906.04644
Turbet, M., Bolmont, E., Leconte, J., et al. 2018, A&A, 612, A86
Turbet, M., & Forget, F. 2019, NatSR, 9, 5717
Turbet, M., Forget, F., Head, J. W., & Wordsworth, R. 2017a, Icar, 288, 10
Turbet, M., Forget, F., Leconte, J., Charnay, B., & Tobie, G. 2017b, E&PSL, 476, 11
Turbet, M., Gillmann, C., Forget, F., et al. 2020, Icar, 335, 113419
Turbet, M., Leconte, J., Selsis, F., et al. 2016, A&A, 596, A112
Wang, S., Sobel, A. H., & Kuang, Z. 2013, JGRD, 118, 6290
Webster, P. J., & Lukas, R. 1992, BAMS, 73, 1377
Wing, A. A., & Cronin, T. W. 2016, QJRMS, 142, 1
Wing, A. A., Emanuel, K., Holloway, C. E., & Muller, C. 2017, SGeo, 38, 1173
Wing, A. A., & Emanuel, K. A. 2014, JAMES, 6, 59
Wordsworth, R., Forget, F., Millour, E., et al. 2013, Icar, 222, 1
Wordsworth, R. D., Forget, F., Selsis, F., et al. 2011, ApJL, 733, L48
Xu, K.-M., & Krueger, S. K. 1991, MWRv, 119, 342
Yang, J., Abbot, D. S., Koll, D. D. B., Hu, Y., & Showman, A. P. 2019a, ApJ, 871, 29
Yang, J., Boué, G., Fabrycky, D. C., & Abbot, D. S. 2014, ApJL, 787, L2
Yang, J., Cowan, N. B., & Abbot, D. S. 2013, ApJL, 771, L45
Yang, J., Leconte, J., Wolf, E. T., et al. 2019b, ApJ, 875, 46
Zechmeister, M., Dreizler, S., Ribas, I., et al. 2019, A&A, 627, A49
Zhang, X., Tian, F., Wang, Y., Dudhia, J., & Chen, M. 2017, ApJL, 837, L27
Zipser, E. J., & Lemone, M. A. 1980, JAtS, 37, 2458